Performance evaluation of inverse methods for identification and characterization of oscillatory brain sources: Ground truth validation & empirical evidences

Tamesh Halder*, Siddharth Talwar*, Amit Kumar Jaiswal, Arpan Banerjee**

Cognitive Brain Lab, National Brain Research Centre, NH 8, Manesar, Gurgaon-122051, Haryana, India

Abstract

Oscillatory brain electromagnetic activity is an established tool to study neurophysiological mechanisms of human behavior using electro-encephalogram (EEG) and magneto-encephalogram (MEG) techniques. Often, to extract source level information in the cortex, researchers have to rely on inverse techniques that generate probabilistic estimation of the cortical activation underlying EEG/ MEG data from sensors located outside the body. State of the art source localization methods such as exact low resolution electromagnetic tomography (eLORETA), Dynamic Imaging of Coherent Sources (DICS) and Linearly Constrained Minimum Variance (LCMV) have over the years been established as the prominent techniques of choice. However, these algorithms produce a distributed map of brain activity underlying sustained and transient responses during neuroimaging studies of behavior. Furthermore, the volume conduction effects and noise of the environment play a considerable role in adding uncertainty to source localization. There are very few comparative analyses that evaluates the "ground truth detection" capabilities of these methods. In this technical note, we compare the aforementioned techniques to estimate sources of spectral event generators in the cortex using a two-pronged approach.

First, we simulated EEG data with point dipole (single and two-point), as well as, distributed dipole modelling techniques to validate the accuracy and sensitivity of each one of these methods of source localization. The abilities of the techniques were tested by comparing the centroid error, focal width, reciever operating characteristics (ROC) while detecting already known location of neural activity generators under varying signal to noise ratios and depths of sources from cortical surface. Secondly, we performed source localization on empricial EEG data collected from human participants while they listened to rhythmic tone stimuli binaurally. Inportantly, we found a less-distributed activation map is generated in LCMV and DICS when compared to eLORETA however, control of false positivesis much superior in eLORETA in realistic distributed dipole scenarios. A comprehensive analysis, further, indicate the strengths and drawbacks of each of the methods.

Key words: EEG, MEG, event related potential, eLORETA, DICS, LCMV, source analysis

*Authors have equal contribution

**

Email address: arpan@nbrc.ac.in,banerjee2007@gmail.com (Arpan Banerjee)

1. Introduction

Cortical oscillations play an important role in governing basic cognitive functions (Edelman and Mountcastle, 1978; Bressler and Kelso, 2001; Buzsáki and Draguhn, 2004). Several researchers have suggested that electromagnetic brain activity at specific frequency bands carries meaningful information about neural function, e.g. alpha waves at 10 Hz (Bollimunta *et al.*, 2008; Llinás *et al.*, 1999), beta at 15-30 Hz (Brovelli *et al.*, 2004), gamma at 30 Hz and above (Bressler *et al.*, 1993; Varela *et al.*, 2001; Cheyne and Ferrari, 2013). Concurrently, time-locked transient responses have been useful for decades in electrophysiological research, both for understanding basic neurobiological functions as well as in clinical and other applications (Picton *et al.*, 1974; Kutas *et al.*, 1977; Pantev *et al.*, 1995; Clark *et al.*, 1995; Cheyne *et al.*, 2006). Hence, identifying the neural generators of sustained cortical oscillations and task-specific transient neural responses from electro-encephalography/ magneto-encephalography (EEG/ MEG) is an extensive topic of research. Once identified with adequate reliability, the focal localization of sources will eventually reveal the underlying large-scale network governing cognitive tasks.

There are several source localization methods that exist in the literature, commonly known under the umbrella of inverse methods (Hämäläinen and Sarvas, 1989). Most of these techniques are based on fitting single/ multiple dipolar cortical source/sources within a defined cortical volume based on some assumptions about relationships between the sources (Van Veen *et al.*, 1997; Gross *et al.*, 2001; Hillebrand and Barnes, 2003; Liu *et al.*, 2002; Sato *et al.*, 2004). Some methods consider sources to have minimum correlation, e.g. synthetic aperture magnetometry (SAM) (Hillebrand and Barnes, 2003), linearly constrained minimum variance spatial filtering (LCMV) (Van Veen *et al.*, 1997; Murzin *et al.*, 2011). There are specialized measures that detect generators of oscillatory brain signals by considering maximum coherence between prospective sources, e.g., dynamic imaging of coherent sources (DICS) (Gross *et al.*, 2001). The aforementioned methods are more popular for MEG, where the possible sources are located closer to brain surface and cost-function optimizations are relatively unambiguous. In EEG, where deeper sources can affect scalp potentials, exact low-resolution brain electromagnetic tomography (eLORETA) (Pascual-Marqui, 2007) has been the method of choice. Though, dynamic statistical parametric mapping (dSPM) (Liu *et al.*, 2002) and sparse Bayesian learning (SBL) (Ramírez *et al.*, 2010) has been developed to improve upon the estimates of spatial filter detection, eLORETA is still by far one of the most robust methods for EEG source localization. eLORETA directly estimates current source density, a biophysically relevant parameter over a grid of plausible cortical locations for both detection of time-locked activity e.g., in event related potentials / fields (EEG/ERF) or frequency-locked activity e.g., spontaneous frequency bursts or steady state oscillatory responses to a periodic stimuli. For example, LCMV is more tuned for detection of ERP/ ERF generators whereas DICS may be considered for spontaneous oscillatory activity that may have large-scale functional connectivity embedded. Nonetheless, the source estimated by all methods are broadly influenced by depth, signal to noise strength of the neural activity in question and redundant informational content of high temporal resolution data. Often these manifest in distributed source activity estimation with diminished statistical power.

The reliability of the location of neural activity along with lower false positives fhould be an important litmus test for any source localization technique. In this article, we evaluate the performance on specificity and sensitivity of the key techniques eLORETA, DICS and LCMV on simulated EEG data. We compared the results from eLORETA and DICS on a paradigm of evoked 40-Hz auditory steady state responses (ASSR) and eLORETA and LCMV for detecting the source of N100 activity when the same data was epoched time-locked to the stimulus onset. Very rigorous comparison metrics e.g. localization error, spatial spread and receiver operating characteristics (ROC) were used to evaluate performance and reliability of results along with a evaluation of the performance of these methods at different depths of dipole placement in the simulated EEG data. The rest of this paper is organized as follows. In Section II, we introduce the simulation framework for testing the three methods (i.e., eLORETA, LCMV, DICS) on synthetic EEG data. We also outline the experimental design used to generate empirical EEG data on which we wish to compare eLORETA, LCMV and DICS. In section III we present the comparative results of applying eLORETA, LCMV and DICS on simulated and empirical EEG data. Finally in section IV we outline comparative benefits and pitfalls of these methods.

2. Materials and Methods

2.1. Generation of synthetic EEG data:

We used a time-varying sinusoid at 40 Hz, plus normally distributed noise as a model for cortical source dynamics. The magnitude of the dipolar source dynamics in cortical locations are represented by

$$q_i(t) = sin(2\pi 40t) + \epsilon(0, \sigma) \tag{1}$$

where $q_i(t)$ is the electric dipole moment at location i and at time t, ϵ is white noise with zero mean and standard deviation σ. We compared 3 conditions with respect to number of sources, by placing single point dipole, two-points dipoles and distributed dipoles in a MNI brain template according to the Montreal Neurological Institute (Müller and Weisz, 2012). Single point source was placed at around the superior temporal region, in the left hemisphere (MNI coordinates: $(-60, -28, 6)$). Two sources were placed, one in the left hemisphere (MNI coordinates: $(-60, -28, 6)$) and the other in the right hemisphere (MNI coordinates: $(64, -24, 6)$) around the superior temporal region. Approximately, hundred point sources were placed within a spherical volume with radius of 12 mm in the left hemisphere centred around superior temporal region at $(-60, -28, 6)$, according to brain template. Another set of hundred point sources were placed around right hemisphere auditory cortex seed area at $(64, -24, 6)$, defining the distributed source condition. The resolution of the grid chosen for dipole simulation was 5mm and "$ft_prepare_leadfield.m$" code of FieldTrip toolbox was used for this purpose. Dipole moment orientations were assumed to be along the radial direction to retain simplicity. We computed the scalp potentials for EEG at realistic sensor locations by applying a forward model (Mosher *et al.*, 1999; Baillet *et al.*, 2001) with realistic headshape using "$ft_dipolesimulation.m$" of the FieldTrip toolbox (Fig 1).

$$v_r(t) = \mathbf{L}^T(r, \mathbf{r}_q).q(t) \tag{2}$$

where, v is the electric potential at sensor location r, r_q represents all source locations, $\mathbf{L}$ represents the "lead field kernel", $(.)^T$ represents transpose and $q(t)$ is the dipole moment. Synthetic EEG data were generated by varying signal to noise ratio (SNR) at the source space. Physiological SNR was estimated using a statistical measure, $10\log_{10}[\frac{s}{\sigma_b}]$, where s is peak-to-peak amplitude of EEG data during rhythmic auditory stimulation (see Experimental Methods below) and σ_b is the standard deviation of the baseline data. We chose a wide range of SNRs both above and below the estimated physiological SNR level to allow us to evaluate the sensitivity of the all the algorithms. Fig 1 shows simulated EEG activity on scalp surface with bilateral auditory cortical sources. Following (Goldenholz *et al.*, 2009), SNR was computed in decibel(dB) using the following equation.

$$SNR_{dB} = 10\log_{10}\left[\frac{1}{U}\sum_{u=1}^{U}\frac{v_u^2}{\eta_u^2}\right] \tag{3}$$

where U is total sensor count, v is the signal on sensor $u \in (1, 2, \cdots U)$ provided by the forward model for a source with unit amplitude. The sensor space variance $\eta_u^2 = \sigma^2(\mathbf{L}\mathbf{L}^T)_u$.

2.2. Source localization methods

The basic goal of any source localization technique is to compute the dipolar source locations and strengths inside the brain from measurements on the scalp (inverse of equation 2). In other words the objective is to estimate the spatial filter $\mathbf{W}_S$ from the relation

$$q(t) = \mathbf{W}_S{}^{\cdot}\ \mathbf{V}(t) \tag{4}$$

where, $q(t)$ is the dipole moment at time t, $\mathbf{W}_S$ is the spatial filter matrix, and $\mathbf{V}$ is vector representation of all sensor time series. Obviously, the system of equations represented by equation 4 is ill-posed as number sensors (dimension of vector $\mathbf{V}$) is finite, but number dipoles are unknown. So, different source localization methods attempt to estimate the $\mathbf{W}_S$ using diverse constraints posed by anatomy of the brain and functional relationships among brain areas during ongoing task.

2.2.1. LCMV

Linearly constrained minimum variance (LCMV) belongs to the class of "beamformer" methods that enhances a desired signal while suppressing noise and interference at the output array of sensors (Barnes and Hillebrand, 2003). LCMV is built upon an adaptive spatial filter whose weights are calculated using covariance matrix of EEG/MEG time series data. A spatial filter computes the variance of the total source power which is allowed to vary but the output of the filtered lead field is kept constant. As a result the beamformer output is maximized for the target source but other source contributions are suppressed. LCMV attempts to minimize the beamformer output power

$$\mathbf{P} = \mathbf{W}_S^T\mathbf{C}\mathbf{W}_S \tag{5}$$

where $\mathbf{C}$ is the data covariance matrix. The entries to spatial filter matrix can be expressed as

$$\mathbf{W}_S = \frac{\mathbf{L}^T\mathbf{C}^{-1}}{\mathbf{L}^T\mathbf{C}^{-1}\mathbf{L}} \tag{6}$$

where L is lead field matrix, and following constraint is maintained $\mathbf{W}_S{}^{\cdot}\mathbf{L}^T = 1$.

2.2.2. DICS

Dynamic imaging of cortical sources (DICS) beamformer (Gross *et al.*, 2001) works with same constraint assumption of LCMV but extends the computation of spatial filter to the frequency domain. Here, sensor level cross spectral density (CSD) matrix replaces the covariance matrix and the spatial filter is applied to sensor level CSD to reconstruct the source level CSD of all combination of pairwise voxels. Hence, DICS directly estimates the interaction between sources at respective frequencies. The weight function can be written as

$$\mathbf{W}_S(f) = \frac{\mathbf{L}^T\mathbf{C}^{-1}(f)}{\mathbf{L}^T\mathbf{C}^{-1}(f)\mathbf{L}} \tag{7}$$

2.2.3. eLORETA

Exact low resolution electrical tomography (eLORETA) (Pascual-Marqui, 2007) combines the lead-field normalization with the 3D Laplacian operator under the constraint of smoothly distributed sources. Compared, to DICS and LCMV where the constraint equation $\mathbf{W}_S{}^{\cdot}\mathbf{L}^T = 1$ is used, eLORETA seeks to minimize the product $\mathbf{H} = \mathbf{W}_S{}^{\cdot}\mathbf{L}^T$.

$$\mathbf{W}_S = [\mathbf{L}^T(\mathbf{L}\mathbf{C}^{-1}\mathbf{L}^T + a\mathbf{H})^{+}\mathbf{L}]^{1/2} \tag{8}$$

where 'a' is regularization parameter, + is the Moore-Penrose pseudo-inverse which is equal to the common inverse if the matrix is non-singular. $\mathbf{H}$ is also called the centering matrix or the surface Laplacian.

Low resolution imaging results in weak performance for recovering of multiple sources when the point-spread functions of sources overlap. Other methods have also tried to combine surface Laplacian with LCMV (Murzin *et al.*, 2013), to estimate source-level connectivity.

2.3. Measurements used for face validity of inverse algorithms:

Using simulated data to test a method provides mechanism for ground truth validation. The exact location of a putative dipolar source is elusive in nature for real data, however, one can certainly set-up simulations when performance of a particular method needs evaluation. We employed three complementary measures to provide face-validity of the eLORETA method with two other methods i.e., LCMV and DICS.

1. Centroid error estimation: Inverse methods estimate a cluster of point dipolar sources. To measure how much error is involved in source localization, we identified the activated voxels in the top 0.5 percentile of all voxel intensities and measured the Euclidean distance between the centroid of the estimated source coordinates and the actual source coordinate, to give us the 'Centroid Error'. This was done for each hemsiphere, separately. Subsequently, the net centroid errors are computed by summing up across two hemispheres and compared for eLORETA, LCMV and DICS.
2. Degree of Focal localization: The size of the cluster in terms of sum of distances of all points from the centroid, gives a measure of focal localization of sources. We computed the total sum of distances of each voxel with significant current density from the centroid location as a measure of the spatial distribution of the estimated source. This gave us a quantitative approach to evaluate the degree of focal source

localization. For practical reasons, cluster width computation was done for each hemisphere separately Murzin *et al.* (2013).

3. Performance evaluation at various depths: The localization of deep sources has been the main factor limiting detection of true sources from M/EEG data. This is highly significant since deep cortical areas constitute 30% of the cortical sources (Hillebrand and Barnes (2002)). We stduied the effects of depth by positioning the dipoles at different distances from the auditory cortical locations mentioned earlier. The depth was varied along the x-axis, from 1 to 20 mm in stepd of 1 mm, towards the center of the brain, in both hemispheres. Further, we computed the centroid error and the focal width of the significant voxels obtained by localizing the dipoles placed at each depth. For the depth analysis, noise was kept to zero to retain simplicity.
4. Receiver Operating Characteristic (ROC) analysis: We compared the "sensitivity" and "specificity" of eLORETA, LCMV and DICS, using receiver operating characteristic (ROC) analysis (Metz, 1978). Here, probability of correct detection, also called 'true positive (TP)' ratios are plotted against a function of probability of incorrectly detecting an activation, also called 'false positive (FP)' ratios. Ideal detection should have enhanced TP while suppressing FP. Hence, a steeply rising ROC curve indicates better performance in terms of sensitivity (higher TP) and specificity (lower FP). We performed ROC analysis on estimated source voxels which are within a certain distance threshold 25 mm (Region Of Interest) from the actual sources (Left and Right Superior Temporal Gyrus). TP is the fraction of significant voxels within the Region of Interest (ROI) at different thresholds ranging from 50 to 95 percentile of all activated voxels. FP is the fraction of significant voxels at the corresponding thresholds that reside outside the ROI. We also compare the performance of all methods under parametric variation of signal to noise ratio at the source level and different kinds of source configurations, e. g., single point dipole, 2-point dipoles and distributed dipoles.

2.4. Empirical EEG recordings

Participants

10 healthy volunteers (8 males, 2 females) aged between $22 - 39$ years (mean age 28 years) participated in the study after giving informed consent, following the guidelines approved by Institutional Human Ethics Board at National Brain Research Centre. All participants were self-declared normal individuals with no history of hearing impairments, had either correct or corrected-to-normal vision and no history of neurological disorders.

Stimuli

Volunteers had to remain stationary in a seated position within a sound-proof room and hear auditory stimuli through 10 Ohm insert earphones with disposable foam ear-tips, binaurally for 200 seconds while fixating at a visual cross. Additionally they had a baseline block where they fixated at the visual cross for 200 seconds without any sounds being played. Sounds were pure tones of 1000 Hz frequency and 25 millisecond time duration, with 5% rise and fall and were repeated with a frequency of 40 Hz during an On block of 1 second duration

interspersed between 2 Off blocks where no auditory stimuli were presented. Stimuli was made using in STIM2 stimulus system with audio box P/N 1105 at 85 dB.

Data Collection and Pre-processing

EEG data was acquired in an acoustically shielded room with 64 channels NeuroScan (SynAmps2) system with 1 KHz sampling rate. Brain Products abrasive electrolyte gel (EASYCAP) was used to make contact with scalp surface and the impedance was maintained at values less than $5k\Omega$ for all volunteers. Baseline EEG data was recorded for 200 seconds with eyes open, no tone, and a fixation cross on a monitor in front of the participants. Baseline and binaural stimuli were presented while participants were asked to maintain fixation on the cross all along to reduce eye movements. A Polhemus Fastrak system was used to track the location of sensors on the EEG cap.

Recorded raw data was re-referenced to linked mastoids (M1 and M2) and was detrended to remove linear trends from the signal. Epochs of 5 second duration were constructed after removing an initial 50 seconds of the 200 seconds long session to capture auditory steady state response (ASSR). Data was band pass filtered with cutoff frequencies 5-48 Hz, to concentrate on sources underlying ASSR.

For an evoked waveform analysis, after re-referencing to linked mastoids (M1 and M2), epochs of 1 second duration during were extracted from the raw data during stimulus condition, then filtered with cut-off frequencies 0.5-48Hz, detrended and averaged across trials to generate the evoked potential. Thresholds of $-100\mu V$ and $100\mu V$ were used to reject blink-corrupted trials, meaning if at any point within the epoch, the voltage exceeded the threshold values, the entire trial was deleted from the subsequent analysis.

Individual sensor locations from the EEG cap (Polhemus) was acquired for each subject. Structural T1-weighted MPRAGE scan was performed on the volunteers using a 3T Philips Achieva MRI scanner for co-registration with the sensor locations for accurate source localization. A forward model for each volunteer was computed using Boundary Element Method (BEM) from their respective T1-image. After computing the lead field intensities in each volunteer, the individual grids were interpolated and finally normalized to a Montreal Neurological Institute (MNI) template. The normalized grid locations where the lead field intensities were exceeding the top 99.5 percentile across all grid locations were characterized as significant sources of brain activity.

3. Results

3.1. Simulated EEG data

Simulated EEG data was computed by placing electric dipolar sources at auditory cortical locations, according to single dipole condition, two-points dipoles condition and distributed dipole condition, using equation 1 and projecting the source activity at realistic sensor locations of a Neuroscan (Compumedics Inc, USA) EEG cap using a realistic head model (equation 2, Baillet *et al.*, 2001). We considered two types of temporal profiles for source activity, a sinusoidal signal mimicking the band-specific frequency response observed in typical

EEG signal such as auditory steady state response (ASSR) and a mixture of Gaussian pulses representing the time-locked event related potentials (ERP). Baseline data set was generated separately by placing sources at the right frontal lobe (10, -69, 36) and the left parietal lobe (-47, 21, 36) by using only the noise terms of equation 1 for source dynamics. The choice of these specific locations were guided by hypothetical locations of fronto-parietal network components reported in human resting state studies. The definition of baseline condition is critical for computing the source activation maps from power ratios between signal and baseline from each of the localization methods, eLORETA, LCMV and DICS. Two prototype examples of simulated scalp activity during task and baseline are illustrated in Fig 1.

Signal to noise ratio (SNR) at the neural level was parametrically varied using equation 3 from 18.8 to 60.3 dB, given the estimations of physiological SNR being approximately within a range $19 - 30$ dB. Physiological SNR was computed from the empirical EEG data using the definition of Goldenholz *et al.* (2009) (equation 3). Simulated EEG data for each SNR scenarios were analyzed with LCMV, DICS and eLORETA. Fig 2 illustrates combined results from eLORETA, DICS and LCMV algorithms on a brain surface rendered by the MNI brain at SNR 26.8 dB for the distributed dipole model. We applied eLORETA and DICS to perform frequency-locked source analysis on the sinusoidal source data. eLORETA and LCMV were employed for localizing the sources of the peak negative response on the gaussian signaal, by selecting a time segment constituting of points ± 25 ms around the peak (Fig 1b). We considered 5 % regularization for each method. Identical inverse filters were used for localizing the oscillatory signal as well as the baseline data. The top 0.5 percentile of the voxels having the highest power ratios were considered significant. For plotting activations, the source locations in the 3-D voxel space was projected to a surface plot using customized MATLAB codes (coord2surf.m in **GitHub location**).

The centroid error was computed by first defining each voxel as point in a cluster and thereby determining the distance of the centroid of cluster points from the true dipole source in each hemisphere. For distributed dipolar sources, the centre of the spherically distributed source was considered as the true dipole location. The average of sum of distances of all such points to the centroid normalized by the total number of points was used to quantify the focal localization of sources, in each hemisphere. All voxels were then transformed to their nearest projections on the cortical surface and identified as possible source locations in Fig 2. The quantitative evaluation of the performances of these inverse methods are addressed as follows.

Accuracy:

Frequency analyses using eLORETA and DICS yielded similar centroid errors for 1-point dipole condition at all SNR levels (Fig 3a). For 2-point and distributed dipoles condition, DICS seems to perform slightly better in high noise scanrios but eLORETA performance was improved when SNR became more favourable (Fig 3b,c). For 1-dipole source, increasing SNR improved detection accuracy but no such benefit is practically observed for 2-dipole though in, distributed dipole condition eLORETA performance got better with increasing SNR.

In time domain analysis, LCMV yielded a lower centroid error for point dipoles (single and 2-point sources) as well as distributed dipoles compared to eLORETA in physiologically realistic SNRs (Fig 3). Interestingly, LCMV performance seemed to be least affected by SNR changes based on the centroid error metric.

Localization Spread:

To measure the degree of focal localization of sources we computed the distance between centroid of estimated source cluster and each significant voxel point contained within the cluster. The average sum of distance across all voxels gives us a measure of focal source localization performance for eLORETA, DICS and LCMV algorithms (Fig 4). eLORETA clearly performs favorably (more focal localization) than DICS and LCMV for most noise settings for single dipole localization. For physiologically relevant noise settings in 2-dipoles and distributed dipoles scenario the performance difference between eLORETA and DICS in frequency domain and eLORETA and LCMV in time domain, were somewhat comparable but overall, eLORETA can claim a more favourable performance.

Depth:

To quantitatively measure the localizing capabilities of eLORETA, DICS and LCMV, source localization was executed for distributed dipoles at different depths. The centroid error and the focal width were computed for the significant voxels. The depth of dipolar locations was varied along the x-axis according to the MNI template, $1mm$ apart for each localization iteration. The deepest positions were selected as [-40. -28, 6] in the left hemisphere and [40, -24, 6] in the right hemisphere. The locations closest to the surface were chosen as [-60, -28, 6] in the left hemipshere and [60, 28, 8] in the right hemisphere.
The centroid error for DICS and LCMV is observed to decline to a greater extent, compared to eLORETA, as we increase the depth of the simulated dipoles. However, the focal width of significant voxels increases with increase in depth of the dipoles. Further, the focal width of sources computed by eLORETA are lesser than that of DICS and LCMV for most depths. Since, no noise was added to the simulated sinusoidal signal or the gaussian pulse, eLORETA can be credited to have a higher degree of focal localization in comparison to LCMV and DICS at zero noise condition.

Sensitivity and Specificity:

To evaluate sensitivity, we computed the Receiver Operating Characteristics (ROC) curves (Fig 6) after applying DICS, LCMV and eLORETA methods in different SNR scenarios across different dipole conditions. The region of interest (ROI) for assigning true positives was fixed at 25 mm (see section 2.3 for details). The leadfield intensity thresholds were chosen from $50th$ to $95th$ percentile of the intensities observed (absolute value was used at steps of 5), to calculate the true positive fraction. Correspondingly, the false positive fraction was determined by the ratio of the significant voxels outside the ROI and total voxels outside the ROI.

A steeper ROC curve is associated with optimal performance as reflected by lower false positives and higher true positives. We observe that eLORETA performance improves with SNR levels, i.e, eLORETA performs better at low noise settings. Interestingly, eLORETA performance improved for distributed dipoles in frequency analysis and time-lock analysis, whereas for DICS and LCMV the performance deteriorated. For point dipole conditions, LCMV performed better than eLORETA for lower SNR values, but eLORETA was way ahead at

higher SNR values. An important observation was that the LCMV performance was least affected by SNR in point dipole conditions which is in line with the results from other metrics of accuracy and localization.

Table 1 classifies the performance of all the methods based on accuracy, localization and sensitivity across all dipole conditions for localizing 40 Hz sinusoidal signal (frequency analysis) and Gaussian pulse response (time-lock) respectively.

3.2. Empirical EEG data

Source localization underlying 40Hz EEG activity

The Fourier spectrum of each EEG channel time series were computed by multi-taper method with number of tapers = 2, using Fieldtrip function ft_freqanalysis.m. Power spectral density of empirical EEG data and the event related potential (ERP) time locked to the onset of a single tone stimulus are shown in Fig 7. Fig 7 a), the topoplot of the difference in power between binaural and baseline conditions at 40 Hz is shown along with the log of power across all trials at sensor Cz. There are peaks at alpha band 8-12 Hz in both binaural and baseline conditions (two-sample $t = -0.018, p = 0.95$) whereas the binaural condition had a sharp rise in power at 40 Hz which was significant (two-sample $t = 0.18, p < 0.0001$). The t-tests were performed on logarithm of power spectrums from two conditions within a frequency bands, $8 - 12$ Hz for alpha and $39.8 - 40.2$ Hz for evoked 40 Hz.

Lead field intensity was computed using eLORETA and DICS by co-registration of Polhemus data and structural MR image, for each participant, which was later normalized to a MNI template (see Methods for details). We considered 5 % regularization for all methods. The ratio of source power between stimulus and baseline condition was calculated in each voxel. The averaged lead field intensities across all participants were evaluated using non-parametric statistics and top 0.5% voxels were identified as sources. In Fig 8a, the left, top, bottom and right views of activation are shown where red regions represent sources from eLORETA analysis while green regions represent activation plots generated by DICS. The yellow regions are where both methods agree about the location of a source.

Acknowledging the absence of ground truth concerning true sources that exist in empirical data, we assumed that the voxels identified as overlapping sources by both the methods i.e., eLORETA and DICS (marked yellow in Fig 8a), to be the "true sources". 7 such clusters and their respective centroids were identified. In parallel, we performed a k-means clustering on all the voxels identified from two methods in question, and identified the cluster of voxels that contained the "true sources". The Euclidean distance between the centroid of the "true source" assigned earlier were computed from each point of this cluster. The normalized sum of distances expresses the focal width of the corresponding method and gives a measure of uncertainty from the method under investigation. The focal width of 7 such clusters and their respective locations are tabulated in Table 2a. Overall, DICS yielded lower cluster widths in comparison to eLORETA

Source localization of N100 response

In Fig 7b) we show the ERP responses to the binaural tone and the ERPs in Off blocks (baseline condition), averaged across all trials and participants (grand average). A negative peak around 100 ms post onset of tone stimulus (N100) was observed in the binaural condition with a latency of around 110 ms. The topoplot represents the spatial map of the difference in relative changes of amplitude between ERPs from the the binaural and baseline conditions across all channels and trials.

Next, we computed the underlying source activation during the N100 response using LCMV and eLORETA. In Fig 8b) we plot the source activations (top 0.5% voxels similar to 40Hz case) in epochs of duration 50 ms, within which the 25th ms corresponds to the peak of N100. 7 clusters were observed where both methods agreed about the location of sources (yellow regions of Fig 8b). The locations of these clusters and the focal width obtained from both methods eLORETA and LCMV, following the same lines of reasoning as in 40 Hz, are tabulated in table 2b.

4. Discussion

Currently, multiple source localizing algorithms exist and many more studies have reported the underlying neural generators of temporally fixed events or the plausible networks governing the control of the frequency response observed in the signals of different complexities. However, different inverse methods provide different solutions leading to no agreement of which algorithm is the 'best method'. Therefore, we compared the popular beamformer methods through metrics, to approach this issue.

We compared three methods, eLORETA (Pascual-Marqui, 2007), LCMV (Van Veen *et al.*, 1997) and DICS (Gross *et al.*, 2001) using the metrics (Centroid error, Focal width, ROC) explained in section 2.3 across three dipolar models (single, two-point and distributed model) for the simulated sinusoidal signal (mimicking the steady state 40 Hz) and a mixture of Gaussian pulses (representing the time locked potential). The models were simplistic, however, since we knew the exact location of dipole/s, ground truth validation was possible. Moreover, the study was conducted across different SNRs to test the each method's sensitivity to noise. In addition, for testing the inverse methods with respect to dipolar depth, we computed centroid error and focal width of significant sources of distributed dipoles placed at different depths for both types of signals, at zero noise condition. Also, we conducted source localization by collecting empirical EEG data exhibiting 40 Hz auditory steady state response, Fig 7. DICS and eLORETA were used to compute the sources underlying the 40 Hz activity and LCMV and eLORETA were used to compute the sources underlying the N100 response, shown in Fig 8.

A general consensus emerges from comparing the algorithms that there is no clear winner (Table 1). DICS performs better than eLORETA in single and two-point dipole conditions, even at lower SNR. The centroid error and focal width of both the algorithms are comparable across all models, but eLORETA shows significant control on the false positive ratio in the distributed dipole condition, proving to be the method of choice for estimating sources underlying frequency response. For time-locked localization, LCMV proved to be a better

option when dealing with noisy data. Performance of DICS and especially, LCMV were observed to be inert to varying SNRs, as opposed to eLORETA. However, it can be inferred that localizing more number of dipoles leads to a reduction in the true positive fraction of LCMV and DICS. On localizing deeper sources, focal width of the cluster increased, but overall, eLORETA proves to be more focal than the other two algorithms in zero noise conditions. Although, since eLORETA is susceptible to noise, cluster analysis on empirical dataset suggests that the presence of noise in EEG can affect the focal localization of eLORETA.

Inspite of the kind of tests we have conducted, the choice of method of localization also depends heavily on the what kind of response needs to be localized i.e. different algorithms may be used for localizing coherent signals, subtle signals or band of frequency. Therefore, even if source localizing algorithms have better performance using several metrics, other methods can be used exploratory fashion. Although, with many localizing options on the shelf, it can be essential to find the overlap of anatomical regions using different algorithms, in order to verify cortical sources. Additionally, studies employing methods such as synchronous EEG/fMRI may predict the neural generators with a better accuracy.

Acknowledgement

This study was funded by Ramalingaswami fellowship (BT/RLF/Re-entry/31/2011) and Innovative Young Bio-technologist Award (IYBA), (BT/07/IYBA/2013) from Department of Biotechnology, Ministry of Science & Technology, Government of India.

References

Baillet, S., J.C. Mosher and R.M. Leahy (2001). Electromagnetic brain mapping. *Signal Processing Magazine, IEEE* **18**(6), 14–30.

Barnes, G. R. and A. Hillebrand (2003). Statistical flattening of EEG/MEG beamformer images. *Hum Brain Mapp* **18**(1), 1–12.

Bollimunta, A., Y. Chen, C. E. Schroeder and M. Ding (2008). Neuronal mechanisms of cortical alpha oscillations in awake-behaving macaques. *J Neurosci* **28**(40), 9976–9988.

Bressler, S L. and J A.S. Kelso (2001). Cortical coordination dynamics and cognition. *Trends Cogn Sci* **5**(1), 26–36.

Bressler, S. L., R. Coppola and R. Nakamura (1993). Episodic multiregional cortical coherence at multiple frequencies during visual task performance. *Nature* **366**(6451), 153–156.

Brovelli, A., M. Ding, A. Ledberg, Y. Chen, R. Nakamura and S. L. Bressler (2004). Beta oscillations in a large-scale sensorimotor cortical network: directional influences revealed by Granger causality. *Proc Natl Acad Sci U S A* **101**(26), 9849–9854.

Buzsáki, G. and A. Draguhn (2004). Neuronal oscillations in cortical networks. *Science* **304**(5679), 1926–1929.

Cheyne, D. and P. Ferrari (2013). MEG studies of motor cortex gamma oscillations: Evidence for a gamma "fingerprint" in the brain?. *Front Hum Neurosci* **7**, 575.

Cheyne, D., L. Bakhtazad and W. Gaetz (2006). Spatiotemporal mapping of cortical activity accompanying voluntary movements using an event-related beamforming approach. *Hum Brain Mapp* **27**(3), 213–229.

Clark, V. P., S. Fan and S. Hillyard (1995). Identification of early visual evoked potential generators by retinotopic and topographic analyses. *Human Brain Mapping* **2**, 170–187.

Doesburg, S. M., G. M. Ibrahim, M. L. Smith, R. Sharma, A. Viljoen, B. Chu, J. T. Rutka, O. Snead and E. W. Pang (2013). Altered rolandic gamma-band activation associated with motor impairment and ictal network desynchronization in childhood epilepsy. *PLoS One* **8**(1), e54943.

Edelman, G. and V. Mountcastle (1978). An organizing principle for cerebral function: The unit model and the distributed system. In: *The* M*indful* B*rain*. MIT Press.

Goldenholz, D. M., S. P Ahlfors, M. S. Hämäläinen, D. Sharon, M. Ishitobi, L. M. Vaina and S. M. Stufflebeam (2009). Mapping the signal-to-noise-ratios of cortical sources in magnetoencephalography and electroencephalography. *Human brain mapping* **30**(4), 1077–1086.

Gross, J., J. Kujala, M. Hämäläinen, L. Timmermann, A. Schnitzler and R. Salmelin (2001). Dynamic imaging of coherent sources: studying neural interactions in the human brain. *Proceedings of the National Academy of Sciences* **98**(2), 694–699.

Hämäläinen, M. S. and J. Sarvas (1989). Realistic conductivity geometry model of the human head for interpretation of neuromagnetic data. *IEEE Transactions on Biomedical Engineering* **36**(2), 165–171.

Hillebrand, A. and G.R. Barnes (2002). A Quantitative Assessment of the Sensitivity of Whole-Head MEG to Activity in the Adult Human Cortex. *Neuroimage***16**, 638650.

Hillebrand, A. and G.R. Barnes (2003). The use of anatomical constraints with meg beamformers.. *Neuroimage* **20**(4), 2302–2313.

Kutas, M., G. McCarthy and E. Donchin (1977). Augmenting mental chronometry: the p300 as a measure of stimulus evaluation time. *Science* **197**(4305), 792–795.

Liu, A.K., A.M. Dale and J.W. Belliveau (2002). Monte carlo simulation studies of eeg and meg localization accuracy. *Human Brain Mapping* **16**(1), 47–62.

Llinás, R. R., U. Ribary, D. Jeanmonod, E. Kronberg and P. P. Mitra (1999). Thalamocortical dysrhythmia: A neurological and neuropsychiatric syndrome characterized by magnetoencephalography. *Proc Natl Acad Sci U S A* **96**(26), 15222–15227.

Metz, C.E. (1978). Basic principles of roc analysis. **8**(4), 283–298.

Mohamed, I. S., H. Otsubo, P. Ferrari, R. Sharma, A. Ochi, I. Elliott, C. Go, S. Chuang, J. Rutka, C. Snead and D. Cheyne (2013). Source localization of interictal spike-locked neuromagnetic oscillations in pediatric neocortical epilepsy. *Clin Neurophysiol* **124**(8), 1517–1527.

Mosher, J. C., R. M. Leahy and P. S. Lewis (1999). EEG and MEG: forward solutions for inverse methods. *IEEE Trans Biomed Eng* **46**(3), 245–59.

Müller, N. and N. Weisz (2012). Lateralized auditory cortical alpha band activity and interregional connectivity pattern reflect anticipation of target sounds. *Cerebral Cortex* **22**(7), 1604–1613.

Murzin, V., A. Fuchs and J. A. Scott Kelso (2011). Anatomically constrained minimum variance beamforming applied to EEG. *Exp Brain Res* **214**(4), 515–528.

Murzin, V., A. Fuchs and J. A Scott Kelso (2013). Detection of correlated sources in eeg using combination of beamforming and surface laplacian methods. *J Neurosci Methods* **218**(1), 96–102.

Pantev, C., O. Bertrand, C. Eulitz, C. Verkindt, S. Hampson, G. Schuierer and T. Elbert (1995). Specific tonotopic organizations of different areas of the human auditory cortex revealed by simultaneous magnetic and electric recordings. *Electroencephalogr Clin Neurophysiol* **94**(1), 26–40.

Pascual-Marqui, R. D. (2007). Discrete, 3D distributed, linear imaging methods of electric neuronal activity. Part 1: exact, zero error localization. *ArXiv e-prints*.

Picton, T. W., S. A. Hillyard, H. I. Krausz and R. Galambos (1974). Human auditory evoked potentials. I. Evaluation of component. *Electroencephalogr Clin Neurophysiol* **36**(2), 179–190.

Ramírez, R.R., D. Wipf and S. Baillet (2010). Neuroelectromagnetic source imaging of brain dynamics. pp. 127–155.

Sato, M., T. Yoshioka, S. Kajihara, K. Toyama, N. Goda, K. Doya and M. Kawato (2004). Hierarchical Bayesian estimation for MEG inverse problem. *NeuroImage* **23**(3), 806 – 826.

Van Veen, B.D., W. van Drongelen, M. Yuchtman and A. Suzuki (1997). Localization of brain electrical activity via linearly constrained minimum variance spatial filtering.. *IEEE Trans Biomed Eng* **44**(9), 867–880.

Varela, F., J. P. Lachaux, E. Rodriguez and J. Martinerie (2001). The brainweb: phase synchronization and large-scale integration. *Nature Review Neuroscience* **2**, 229–239.

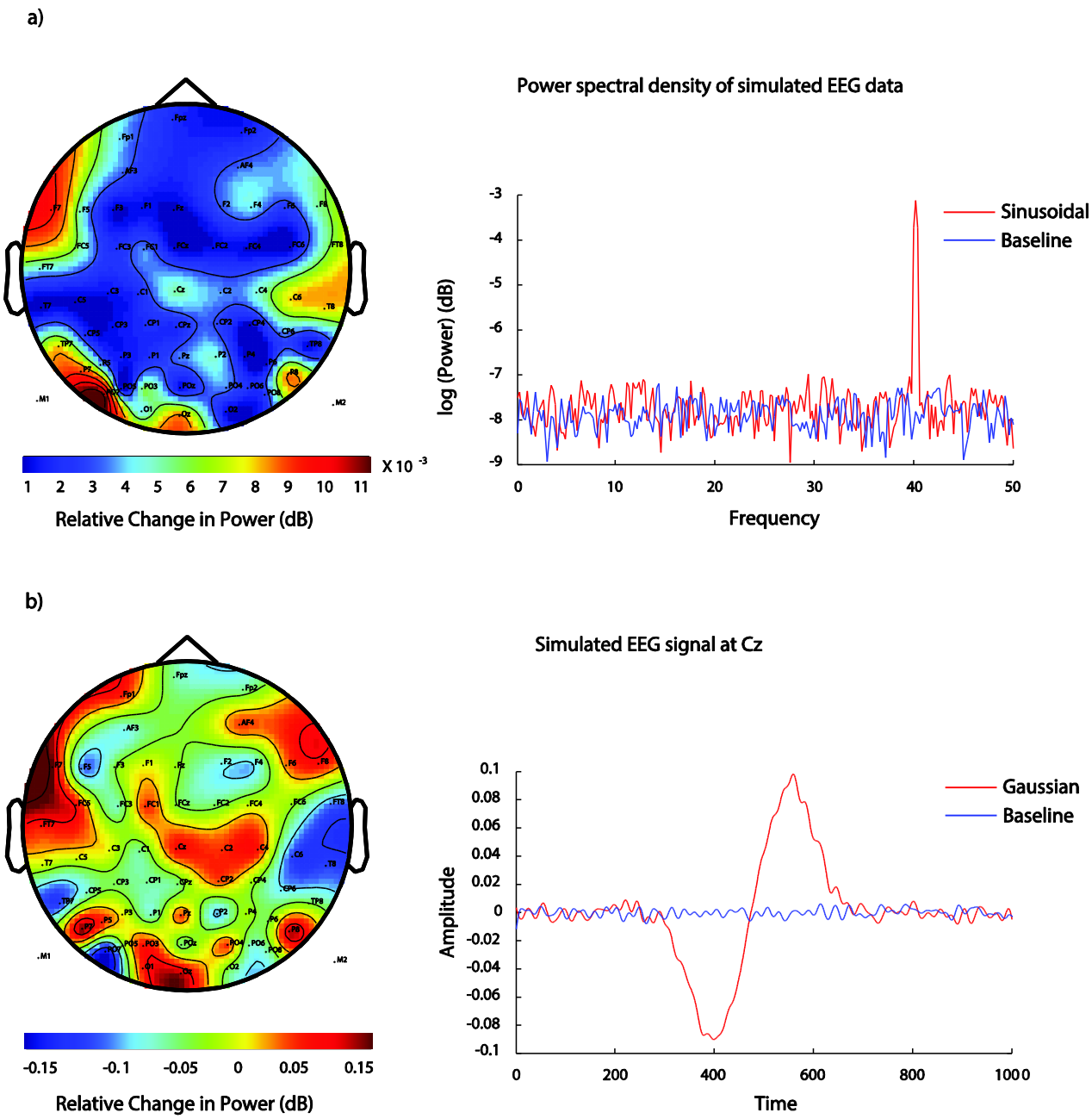

Figure 1: a) Topoplot and log of power of simulated 40 Hz signal shows the difference in power spectral density between the sinusoidal and the baseline conditions. High power at 40 Hz frequency is shown for the sinusoidal signal (in red) in contrast to baseline noise (in blue). b) Topoplot and the simulated transient signal across Cz channel shows the difference in power spectral density between gaussian (in red) and baseline (in blue) conditions. Both are simulated as per the distributed dipole model at SNR of 26.5 dB.

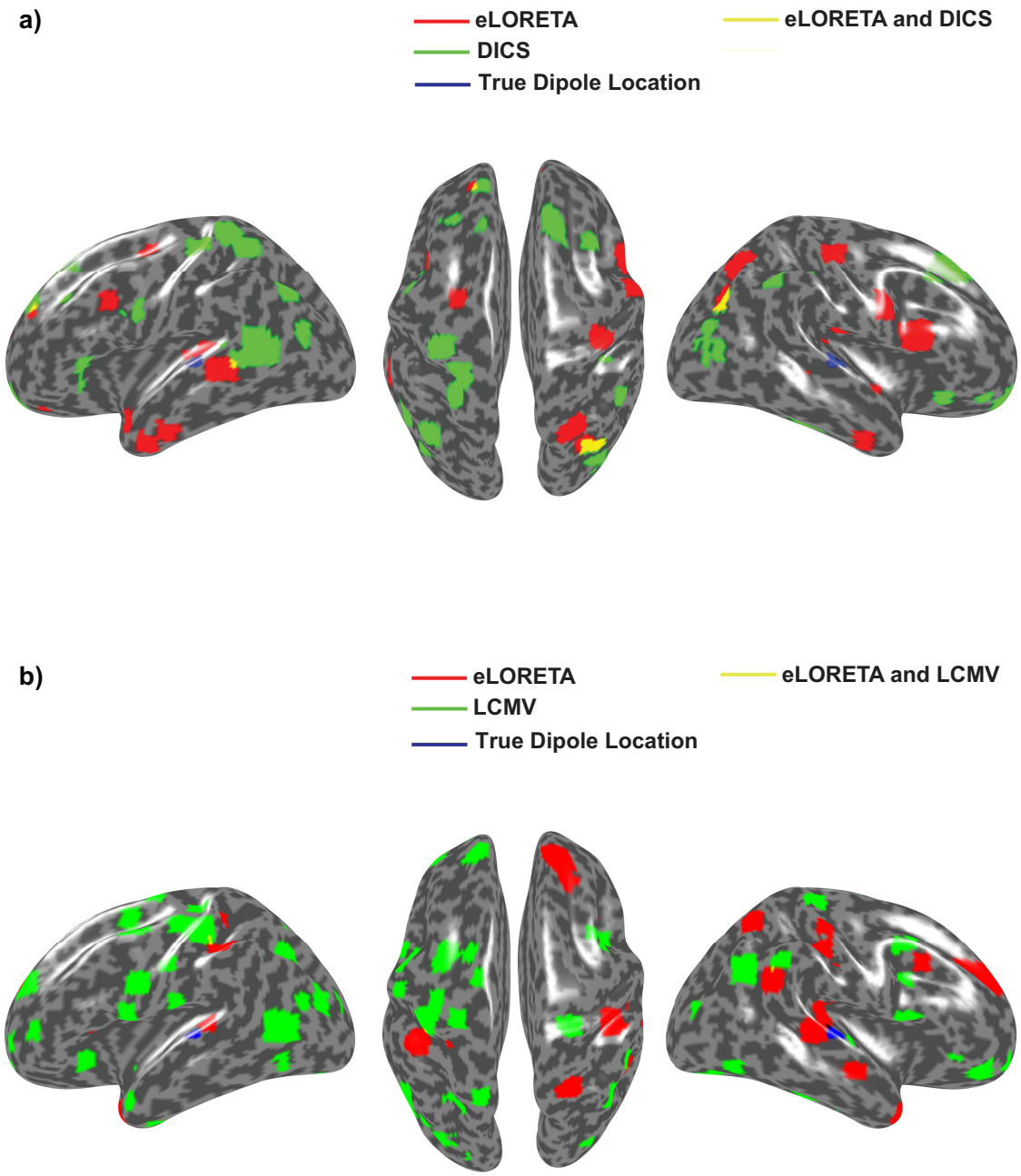

Figure 2: a) eLORETA source localization (red) vs DICS source localization (green) using frequency lock analyses. b) eLORETA source localization (red) vs LCMV source localization (green) using time lock analysis (at threshold level 99.5%, p=0.05). Physiologically realistic SNR 26.3 dB for simulated dipolar sources was chosen for this illustration. True source location is marked as blue dot. Overlapping estimations from two methods areas are shown in yellow, while a overlap of the true dipole location with the estimated locations are marked in black. Distributed dipolar sources are used this example

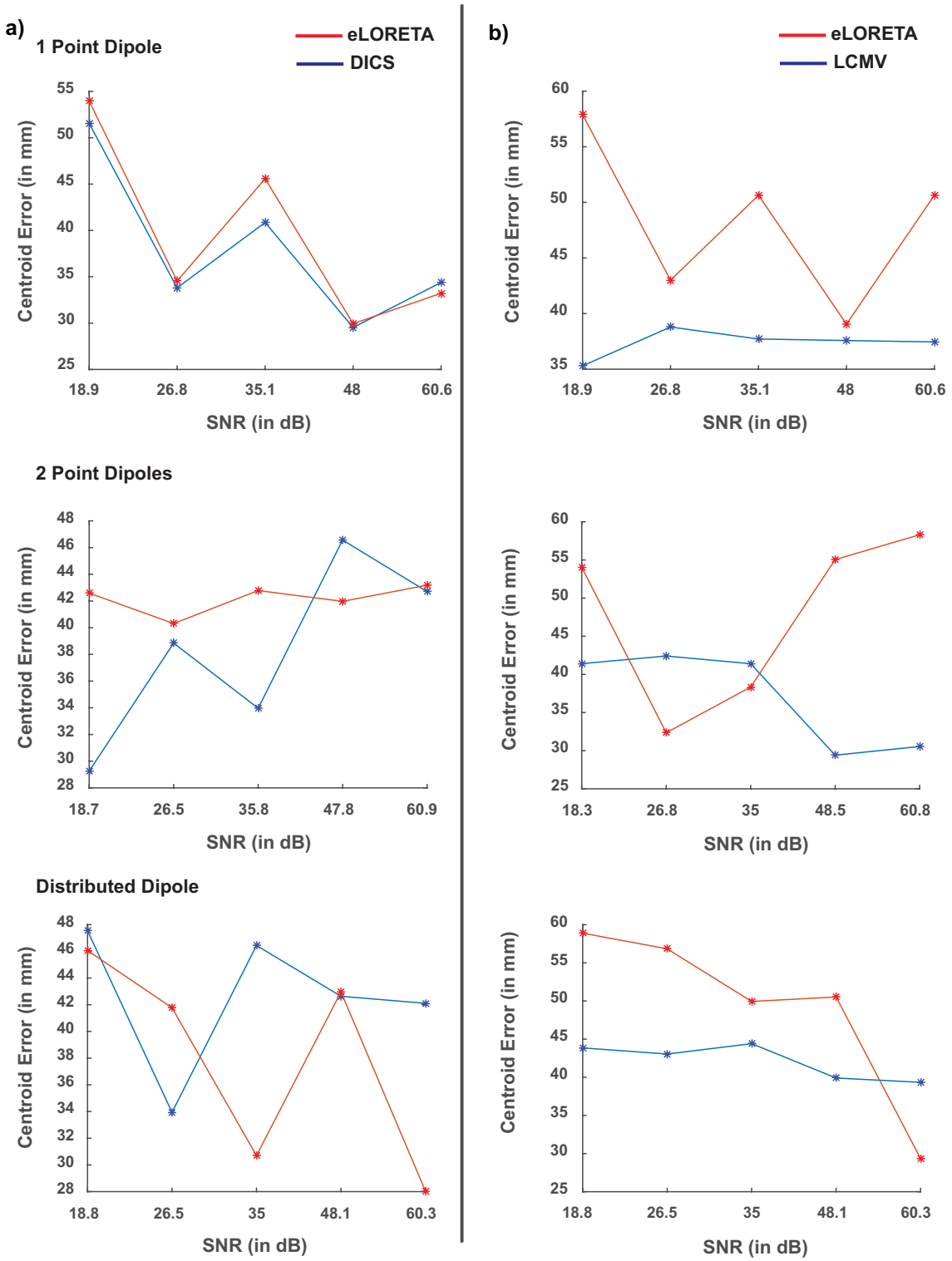

Figure 3: Cumulative centroid errors, i.e., Euclidean distances between centroid of estimated sources to true sources locations, $(-60, -28, 6)$ and $(64, -24, 6)$ (in MNI coordinates) across different SNRs. Centroid error of a) sinusoidal signal and b) Gaussian pulse as dipolar sources.

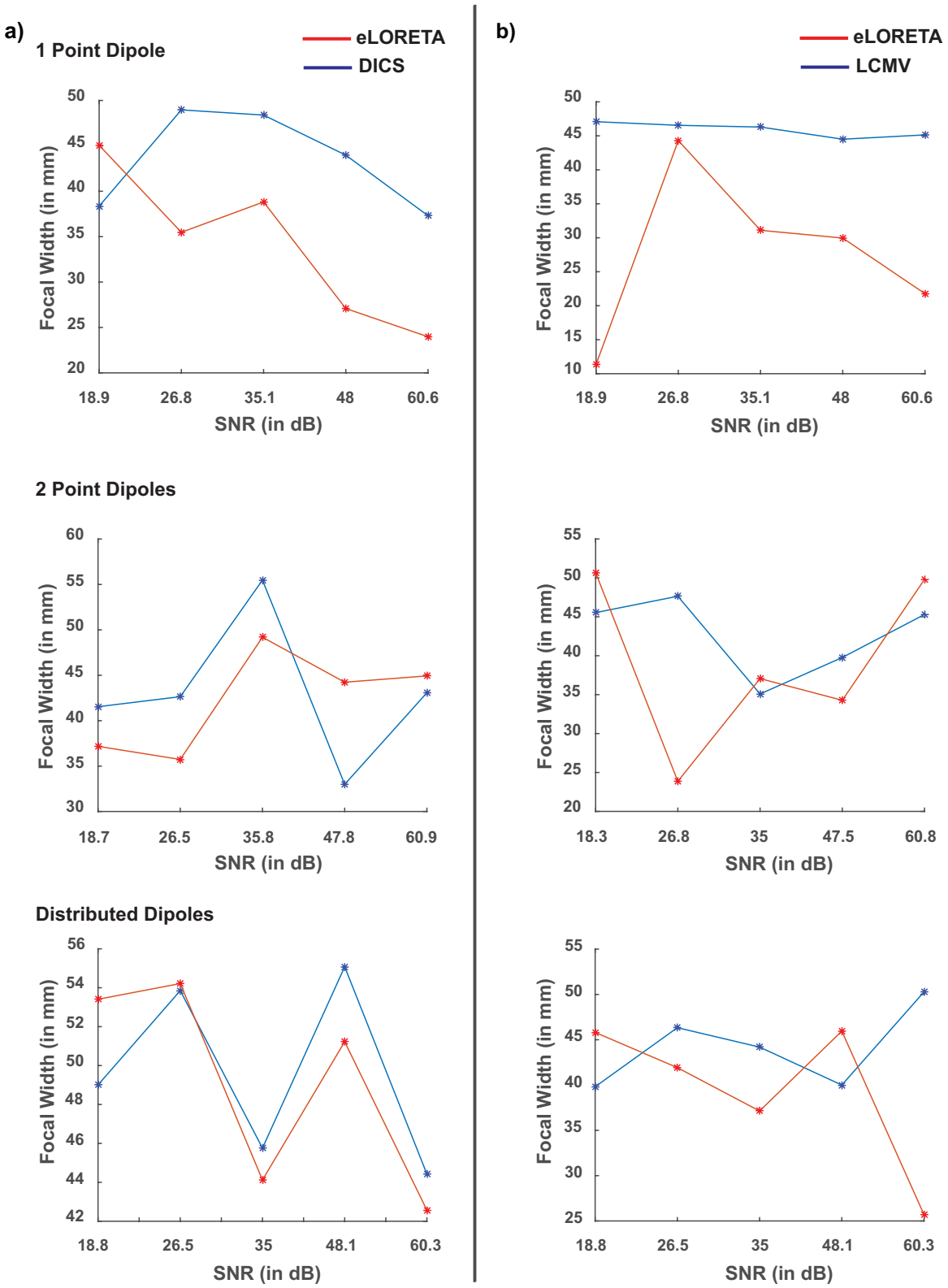

Figure 4: Focal width of detected cortical sources, i.e., the summed distance of all significant voxels (at threshold level 99.5%, $p = 0.05$) from their centroid as a function of different SNRs. Focal error of a) sinusoidal signal and b) Gaussian pulse as dipolar sources.

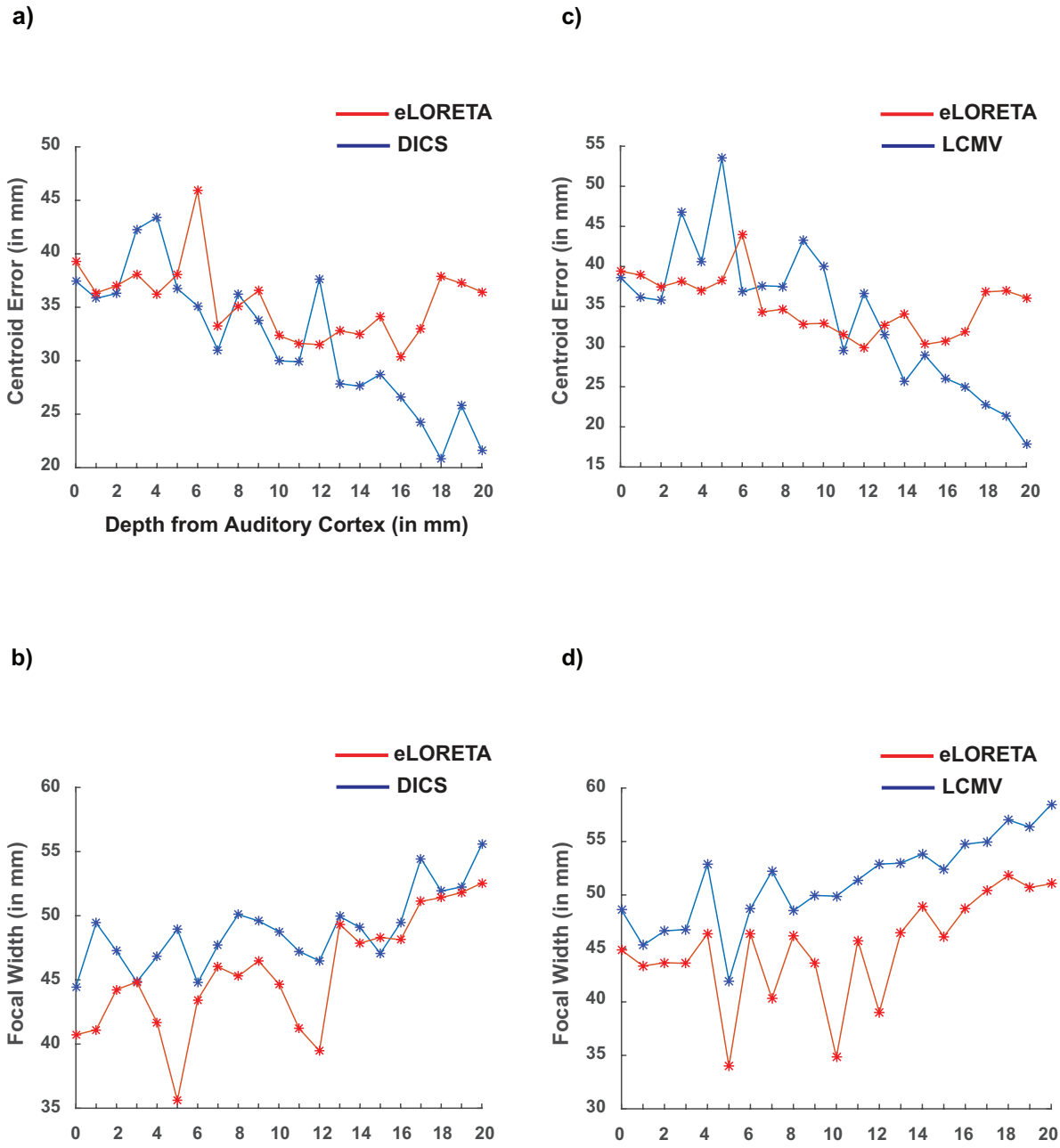

Figure 5: Centroid errors and focal widths of all significant voxels (at threshold level 99.5% $p = 0.05$) computed for simulated distributed dipoles at different depths from the auditory cortical locations LH$(-60, -28, 6$ and RH$(64, -24, 6))$. The depth of the dipoles increases along the x-axis; the distance from the center of the brain. For both sinusoidal signal and gaussian pulse, a), b) centroid error and c), d) focal width of dipolar sources, respectively.

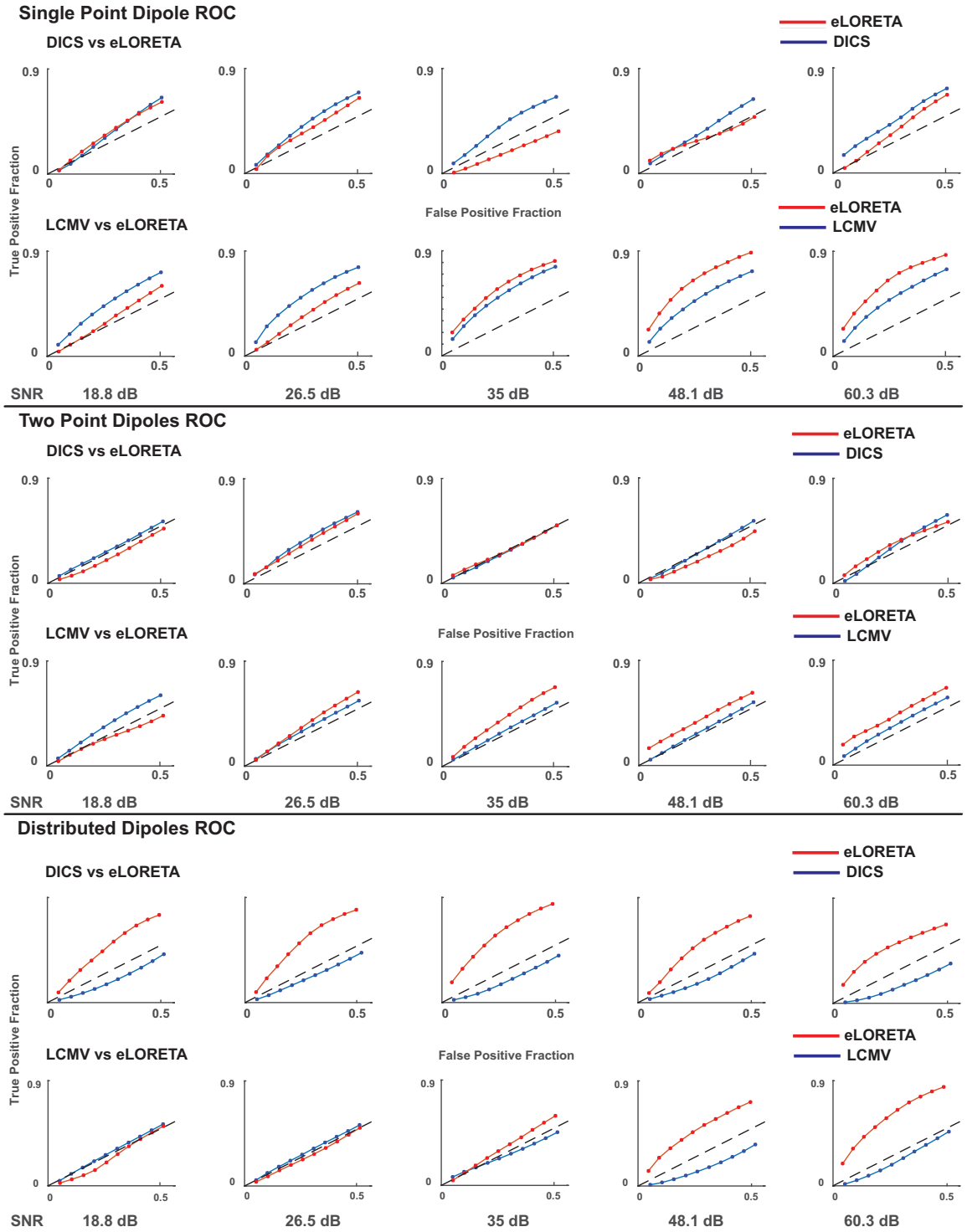

Figure 6: Performance analysis of a) DICS (blue) and eLORETA (red) and b) LCMV (blue) and eLORETA (red) using Receiver Operating Characteristics (ROC) curve based upon different SNR situations. ROC was measured for two different sources, i.e., for for a) sinusoidal signal and b) Gaussian pulse. The curves are plotted with decreasing threshold values along the positive x-axis (Thresholds from 0.95 to 0.5). The black dotted lines indicate ROC curves for chance level detection.

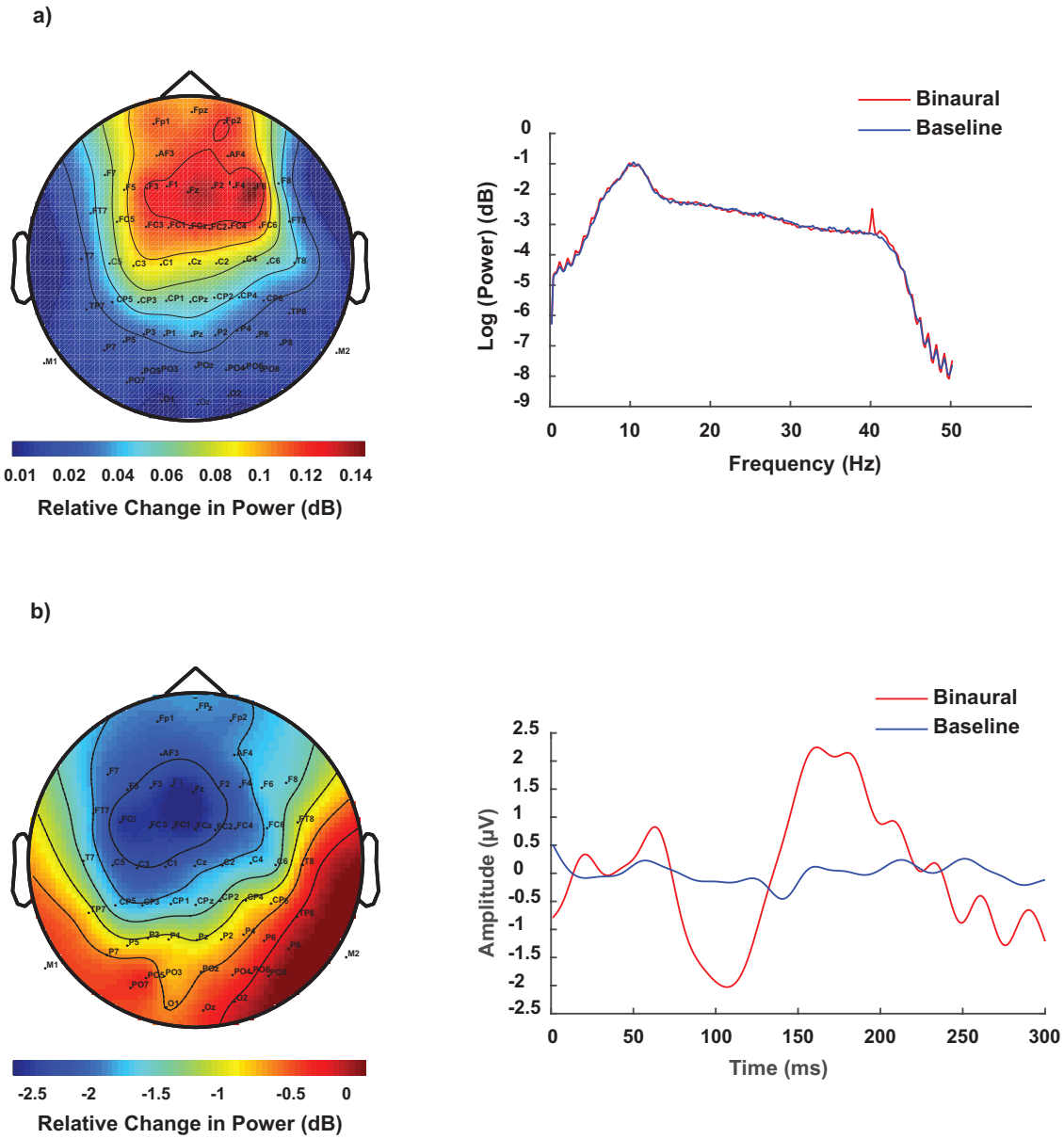

Figure 7: a) Topoplot and frequency response of all channels averaged across all trials of all participants shows the difference in power spectral density between the binaural and the baseline conditions. Power spectral density was calculated for 5 sec windows after rejecting an initial 50 sec in each task condition out of total duration of 200 seconds. b) Group-averaged across channel Cz, the N100 event related potential (ERP) peak of the binaural condition (in red) is plotted in contrast to the baseline condition (in blue), observed in a window of $[0, 150]$ ms post auditory tone onset.

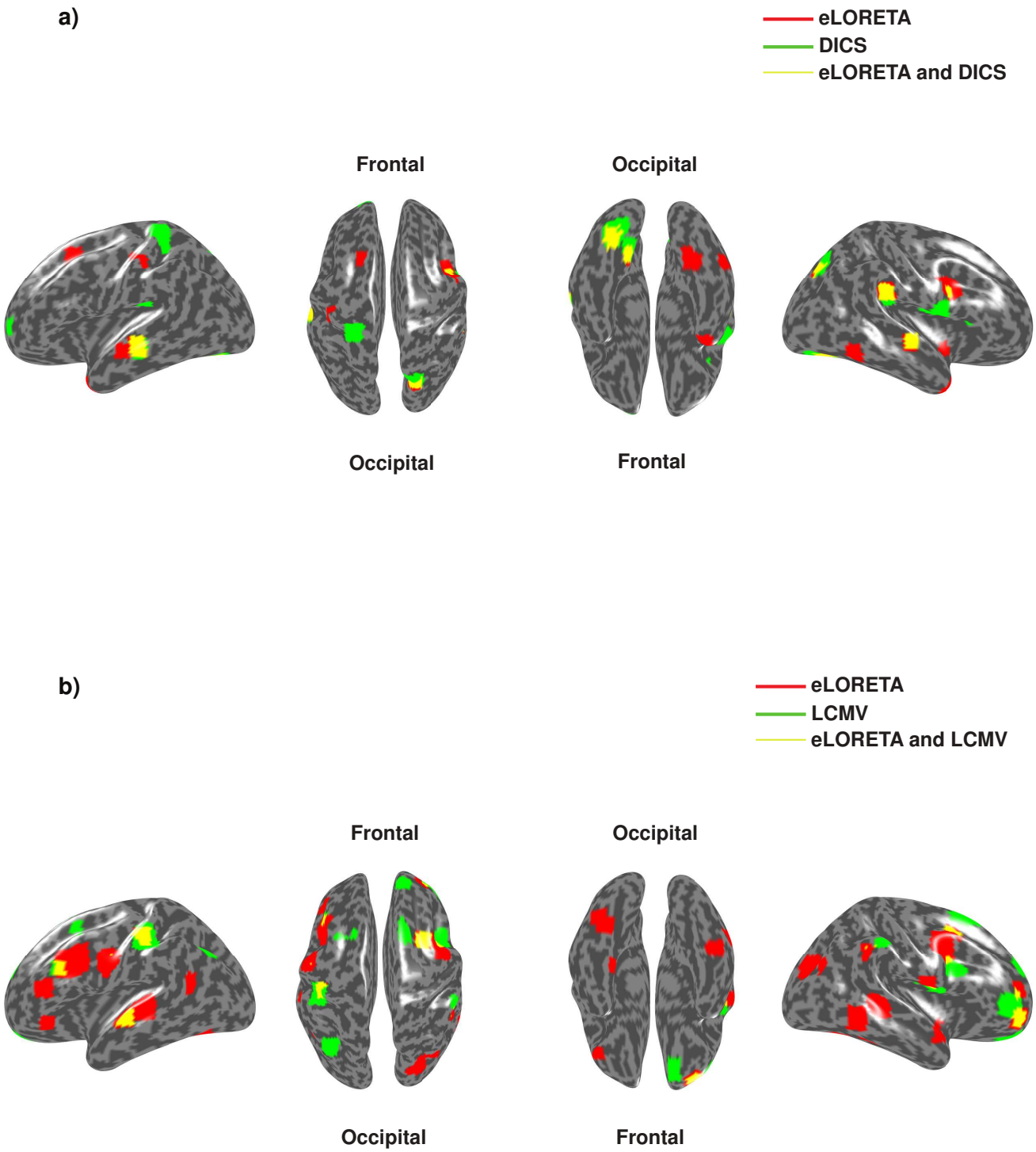

Figure 8: a) Left, top, bottom and right view of cortical activation averaged over all participants for a) 40 Hz activity b) N100 response. The red region shows estimated source by eLORETA while green region shows estimated sources by a) DICS and b) LCMV. Yellow regions mark the overlapping regions computed by both methods.

a) Frequency Analysis			
Dipole Condition	**ROC**	**Centroid Error**	**Focal Width**
Single Dipole	DICS	DICS/eLORETA	eLORETA
Two-point Dipoles	DICS (Low SNR) eLORETA (High SNR)	DICS	DICS/eLORETA
Distributed Dipoles	eLORETA	DICS/eLORETA	DICS/eLORETA
b) Time-lock Analysis			
Dipole Condition	**ROC**	**Centroid Error**	**Focal Width**
Single Dipole	LCMV (low SNR), eLORETA (high SNR)	LCMV	eLORETA
Two point Dipoles	LCMV (very low SNR), eLORETA (moderate to high SNR)	eLORETA/LCMV	eLORETA/LCMV
Distributed Dipoles	LCMV (low SNR), eLORETA (high SNR)	LCMV	eLORETA/LCMV

Table 1: Comparison of source localization performance based on 3 metrics for a) frequency analyses, eLORETA, DICS and b) time-lock analyses eLORETA, LCMV. Both are mentioned with '/' if similar performance was noted.

a) Cluster Width (in mm)			Location
Cluster	**eLORETA**	**DICS**	
Cluster 1	6.9235	1.5926	Right Inferior Frontal Gyrus
Cluster 2	1.7448	1.2955	Right Middle and Temporal Gyrus
Cluster 3	2.6542	2.1674	Right Inferior Parietal Lobule
Cluster 4	3.0514	5.2243	Right Parietal Cortex and Precuneus
Cluster 5	7.3533	5.9084	Left Frontal Cortex (Sub-Gyral)
Cluster 6	6.0342	2.4268	Left Fusiform Gyrus
Cluster 7	1.9577	1.9203	Left Middle Temporal Gyrus
Average Width	4.2455	2.9336	

b) Cluster Width (in mm)			Location
Cluster	**eLORETA**	**LCMV**	
Cluster 1	3.1223	1.117	Right Middle and Superior Frontal Gyrus
Cluster 2	2.7083	1.7867	Right Middle and Superior Frontal Gyrus
Cluster 3	1.3487	2.0031	Right Middle Frontal Gyrus
Cluster 4	2.9609	1.6854	Right Supramarginal Gyrus/Inferior Parietal Lobule
Cluster 5	6.4728	0.654	Left Frontal Cortex
Cluster 6	2.5337	4.501	Left Inferior Parietal Lobule and Parietal Cortex
Cluster 7	4.3125	1.3474	Left Superior Temporal Gyrus
Average Width	3.3513	1.8706	

Table 2: a) Cluster Widths of sources computed by eLoreta and LCMV of the N100 response, along with the respective locations of the clusters. b)Cluster Widths of sources computed by eLoreta and DICS of steady state 40Hz activity and locations of the clusters.